

Numerical modeling of tektite origin in oblique impacts: Implication to Ries-Moldavites strewn field

NATALIA ARTEMIEVA¹ – ELISABETTA PIERAZZO² – DIETER STÖFFLER³

¹Institute for Dynamics of Geospheres, Russian Academy of Sciences, Leninsky Prospect 38/6, Moscow, Russia 117939; e-mail: art@idg.chph.ras.ru

²Planetary Science Institute, 620 N. 6th Street, Tucson, AZ 85705, USA; e-mail: betty@psi.edu

³Institut für Mineralogie, Museum für Naturkunde, Humboldt-Universität zu Berlin, Invalidenstrasse 43, D-10099 Berlin, Germany;
e-mail: dieter.stoeffler@rz.hu-berlin.de

Abstract. On the basis of detailed geological, petrographic, geochemical, and geographical information we have performed a numerical modeling study of three related and coeval impact features: The Steinheim crater (apparent diameter $D_a = 3.8$ km), the Ries crater ($D_a = 24$ km) in Southern Germany, and the moldavite (tektite) strewn field in Bohemia and Moravia (Czech Republic), Lusatia (East Germany), and Lower Austria. The moldavite strewn field extends from about 200 km to 450 km away from the centre of the Ries to the ENE forming a fan with an angle of about 57° . According to this modeling work, an oblique impact of a binary asteroid from a WSW direction appears to be a reasonable working hypothesis to explain the setting of the craters and the formation and distribution of the moldavites. We carried out a series of 3D hydrocode simulations of a Ries-type impact. The results confirm previous results indicating 30° from the horizon as the most probable angle for near surface melting, and, consequently for the formation of tektites. Finally, the simulation of the motion of impact-produced tektite particles through the atmosphere produces a narrow-angle, downrange, distant distribution of the moldavite tektites in a fan-like field with an angle of about 75° . Although the calculated distribution still deviates to some degree from the known distribution of the moldavites, our results represent an important step toward a better understanding of the origin and distribution of the high-velocity surface melt (tektites) and the low-velocity, deep-seated melt (coherent clast-laden melt) resulting from an oblique impact on a stratified target.

Key words: impact crater, tektite, moldavite, melt, numerical modeling, Ries-Moldavite strewn field, Germany, Czech Republic

Introduction

Since 1963 when the first radiometric ages became available (Gentner et al. 1963), there has been a general agreement that the impact craters of Ries and Steinheim (24 and 3.8 km in diameter, respectively), southern Germany, and the moldavite strewn field (Bohemia, Moravia, Lusatia, and Lower Austria, E to NE of Ries and Steinheim; Fig. 1) were formed within a single impact event of some 15.0 Ma (Gentner et al. 1963, Bolten and Müller 1969, Gentner and Wagner 1969, Pohl et al. 1977, Reiff 1979 and references therein, Staudacher et al. 1982, Stöffler and Ostertag 1983, Lange 1996). Regarding the ejection mechanics of moldavites only a few older studies are available (Vand 1963, David 1966). Despite some 40 years of modern research on the three impact phenomena, a comprehensive understanding of the process, which formed the double crater and the tektites in one impact/ejection event, is still lacking.

In this paper, we consider mainly the Ries crater. Because of the large physical separation of the two craters, most probably any interaction between the two simultaneous impact events took place only at a late stage, as shock waves decay rather quickly into seismic waves. In general, shock pressure drops below 0.1 GPa at a distance, which is 50–100 times the projectile radius (Melosh 1989, Ahrens and O'Keefe 1977). It is also improbable that any interaction occurred between the expansion plumes generated by the impacts, as the Steinheim basin is small enough that its expansion plume would decelerate within

one atmospheric scale height (around 8 km). However, the ballistic ejecta of both craters could have interfered with each other. Such effects are probably erased by later erosion although distal Ries ejecta could be searched for in drill cores of the inner breccia lens of the Steinheim basin.

Pre-impact stratigraphy, its simplified model and equation of state

The target rocks of both the Ries and Steinheim craters at the time of impact consisted of a more or less horizontally layered sequence of Tertiary, Jurassic and Triassic sedimentary rocks (limestone, shale, sandstone) and possibly some minor Permian sediments, ~620 m and ~1180 m, respectively, in thickness. This sedimentary rock sequence is underlain by crystalline rocks (gneisses, granites, metabasites) of Hercynian age (about 300 to 350 Ma), e.g. Graup 1978, Hüttner and Schmidt-Kaler 1999.

Only in case of the Ries, the basement is affected by the cratering event. Tertiary sand, clay, and freshwater limestone on top of the Upper Malmian limestone formed a discontinuous layer on the pre-impact surface (0–50 m thick) (e.g. Hüttner and Schmidt-Kaler 1999). Table 1 shows the stratigraphy at the Ries, which has been used to construct a “simplified” model stratigraphy for the hydrocode simulations with ANEOS equation of state (Thompson and Lauson 1972). Modeled target (Table 2) consists of a 600 m thick sedimentary layer divided into,

Table 1. Stratigraphy and lithologies of the Ries pre-impact target (modified from Hüttner and Schmidt-Kaler 1977, 1999)

Stratigraphic sections and thickness (m)*	Subdivisions and lithologies	Thickness (m)*
Tertiary 0–50	Middle Miocene = sands with minor clay and freshwater limestone	0–50
Malmian 150–200	ϵ = massive limestone	~ 20
	δ = massive limestone	70–100
	γ = bedded limestone with some marly limestone, marl and some reef limestone	~ 30
	β = mainly bedded limestone	~ 20
	α = marly limestone, marl, bedded limestone	40–50
Dogger 140–150	γ - ζ = limestone, calcareous limestone and shale	~ 10
	β = sandstone, in part iron-rich	~ 40
	α = gray shale	90–100
Liassic 30	Black shale with some sandstone and marl	~ 30
Triassic 250–300	Upper Keuper = red shale	~ 30
	Middle Keuper = sandstone with some shale	~ 200
	Muschelkalk = calcareous sandstone	0–50
	Buntsandstein ?	up to 15 ?
Hercynian basement	Various gneisses, granites, amphibolites	several km

* Range of estimates for the pre-impact target at the point of impact.

from top to bottom: 40 m of quartzite (ANEOS equation of state from Melosh, personal comm.) with 30% porosity (density of 1.86 g/cm³) to model the uppermost Tertiary sands; 140 m of dense calcite (density of 2.6 g/cm³; Pierazzo et al. 1998) to model the Malmian limestone; 420 m of quartzite with 20% porosity (density of 2.12 g/cm³) to model the Jurassic/Triassic sandstones and shales. The crystalline basement below the sedimentary layer is modeled as non-porous granite (Pierazzo et al. 1997). Since only 3 different materials are currently allowed in SOVA (which allows a rigorous mathematical treatment of mixed cells in the simulations), we model the atmosphere as pure CO₂ (i.e. decomposed calcite), instead of real air. However, we use density-pressure distributions of the Earth atmosphere and believe that this simplification does not influence particle’s motion and, hence, final deposition of tektites. The projectile consists of granite with 5% porosity (corresponding to a bulk density of 2.5 g/cm³).

Distal ejecta of the Ries crater

Large parts of the Ries’ continuous ejecta blanket are preserved consisting of a polymict lithic, clastic matrix breccia (Bunte Breccia, < 200 m thick) covered by "fall-out" suevite patches (polymict clastic matrix breccia with lithic and mineral clasts of all shock stage including impact melt particles derived mainly from the crystalline basement) ranging in thickness from ~5 to 90 m (Stöffler and Ostertag 1983, Engelhardt 1997). Bunte breccia and suevite extend radially to about 45 km and 23 km, respectively (Hüttner and Schmidt-Kaler 1999).

Distal, discontinuous ejecta comprise Upper Jurassic limestone clasts ("Reuter blocks", cm–dm sized; Gall and Müller 1975) and moldavite tektites extending radially between about 50 to 70 km and 200 to 450 km, respectively, from the point of impact (Stöffler and Ostertag 1983, Lange 1996), as shown in Fig. 1. As indicated by its chemical and isotopic composition the moldavite melt originates from the top 50 m of sand-dominated Tertiary deposits of the Ries target, with minor additions of clay and limestone (Engelhardt 1972, Horn et al. 1985, Engelhardt et al. 1987).

Hydrocode modeling

All results presented below relate to the Ries crater and its impact melts, specifically to the initial stage of the Ries crater growth, when the pressures are rather high and allow for simplified hydrodynamic (without material strength) description. This treatment is sufficient for simulating melt production and melt ejection. A complete numerical description of the Ries crater formation, i.e. including crater collapse, would require a detailed treatment of strength and of the rheological properties of the complex Ries target (currently there is no hydrocode that can model accurately both the early and late stages of crater formation).

Impact simulations were carried out with the three-dimensional (3D) hydrocode SOVA (Shuvalov 1999) coupled to a tabular version of the ANEOS equation of state package. SOVA is a two-step Eulerian code that can model multidimensional, multi-material, large deformation, strong shock wave physics. It is based on the same princi-

Table 2. Target layout for the Ries hydrocode modeling (see Fig. 3b)

Material	Depth (km)	Density (g/cm ³)	Porosity (%)	ANEOS	Reference
<i>Tertiary Sands</i>	0.00–0.04	1.86	30	quartzite	MELOSH, personal comm.
<i>Malmian Limestone</i>	0.04–0.18	2.6	0	calcite	PIERAZZO ET AL., 1998
<i>Jurassic/Triassic Sandstone</i>	0.18–0.60	2.12	20	quartzite	MELOSH, personal comm.
<i>Crystalline Basement</i>	0.60–20.0	2.63	0	granite	PIERAZZO ET AL., 1997

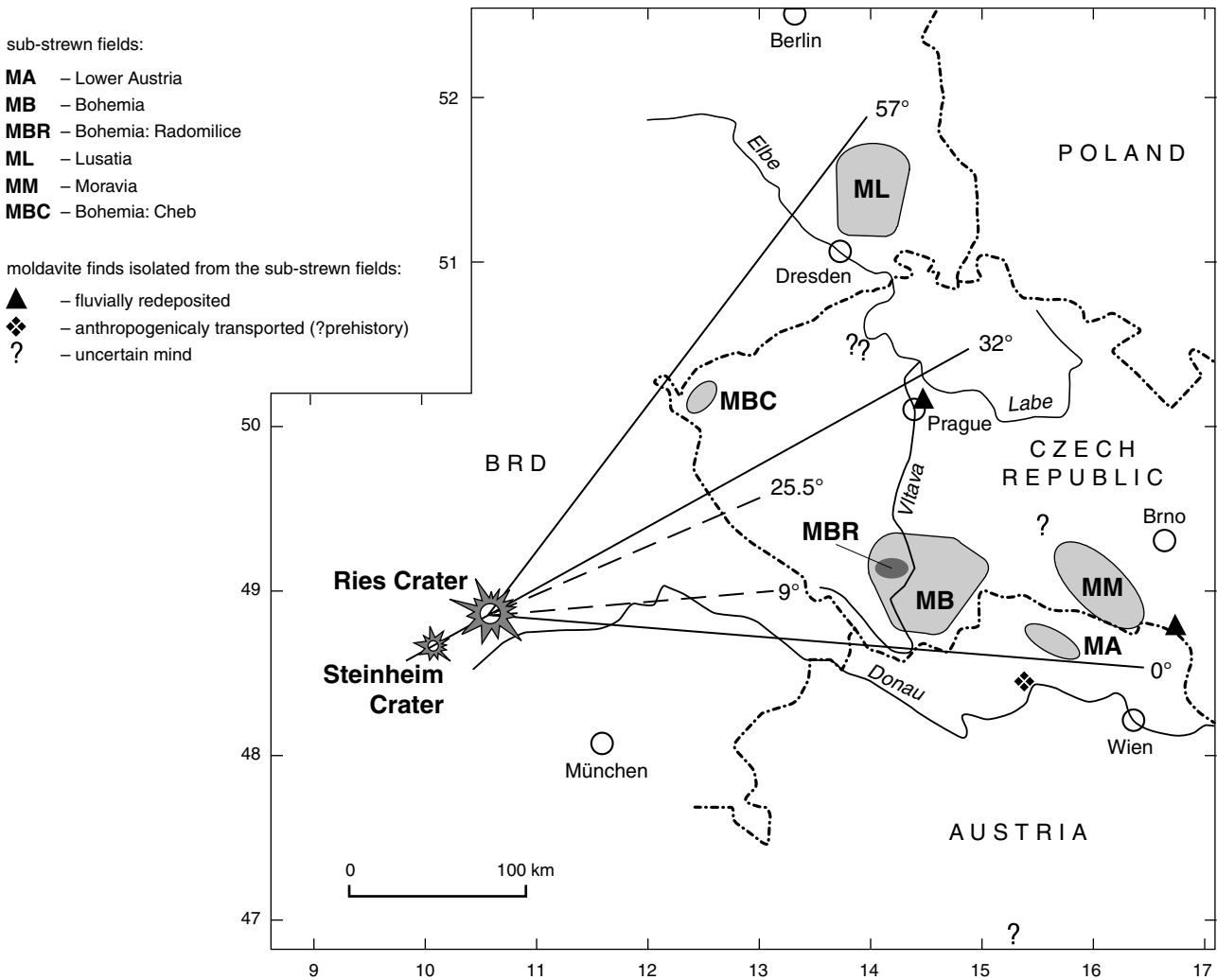


Figure 1. Map of Central Europe showing the Ries and Steinheim craters and the Moldavite strewn field (modified after LANGE, 1996); the sub-strewn-fields are hatched and explained in the legend; dashed lines (9° to 25.5°) define the fan within which coherent melt lumps are observed on the inner slope of the Ries crater rim.

ples utilized in the well-known code CTH (McGlaun et al. 1990). A feature that makes SOVA unique among hydrocodes used for impact cratering studies is the implementation of a procedure to describe particle motion in the evolving ejecta-gas plume, including the interaction of particles with the gas. The algorithm of particle description is presented below in the section *Tektite production*.

The simulations model spherical asteroids striking Earth’s surface at angles of 45° , 30° , and 15° from the surface with velocities of 12, 20 and 40 km/s. To make sure that all the simulations model a similar transient cavity diameter (between 12 and 13 km; Hörz et al. 1983), the projectile sizes were varied according to the Pi-scaling law (Schmidt and Housen 1987), and are shown in Table 3. Spatial resolution was optimized to best represent the target lithology, ranging from 10 m, to resolve the thin surface layers, to 60 m away from the impact site. The use of bilateral symmetry allowed us to model the $y > 0$ half space only, and thus take advantage of the available computer capacity for a higher resolution near the impact site.

Since the simulations start with the projectile close to the surface, we do not consider the atmospheric wake (i.e. the “hole” punched in the atmosphere by the entering projectile) and its interaction with the ejecta. However, this is not an important mechanism for impact angles less than $\sim 75^{\circ}$, as the post-impact flow develops mainly in the downrange direction, opposite to the location of the wake. In contrast, for vertical impact the post-impact flow develops entirely inside the wake (Artemieva and Shuvalov 1994).

Table 3. Amount of melt + vapor (in km^3) produced in the hydrocode simulations for the various target layers

Impact Velocity	12 km/s		20 km/s		40 km/s	
	30°	45°	15°	30°	45°	45°
D_{pr} (km)	1.9	1.6	2.1	1.5	1.2	0.8
Sands (40 m)	0.39	0.21	0.67	0.37	0.23	0.21
Limestone (140 m)	0.98	0.57	2.15	1.14	0.58	0.49
Sandstone (420 m)	5.39	3.73	7.92	6.27	3.77	3.38
Basement	6.70	7.20	9.20	13.44	9.72	8.22
TOTAL	13.46	11.71	19.94	21.22	14.30	12.30

Melt production

Figure 2 shows the early stages of impact ($t \sim 0.5$ s) for a 20 km/s impact at 15°, 30°, and 45° from the surface (projectile was coming from the left). The crystalline basement is shown in gray, quartzite in green, and calcite in dark blue. The atmosphere is shown in blue. All the colors are graded according to density variations. Impact angle affects the melting and early ejection of material from the crater. Figure 2 also suggests that impact angle strongly affects the shape of the opening cavities; however, this is true only for the very early stages of the impact event, but the final crater shape depends on the late stage of excavation and collapse, for which the impact direction is not an important parameter (at least for impact angles exceeding about 15°).

For each simulation, we estimated the amount of melting of the various layers modeled, including the crystalline basement. This has been done by marking each computational cell with a Lagrangian massless tracer particle (representing the given cell) that records the thermodynamic history of the material in the cell. The amount of melting and vaporization is determined by adding up the initial volume of cells whose tracers record shock pressures above a given threshold. We used 55 GPa as the threshold for shock degassing of non-porous calcite (140 m limestone layer). For 30% (upper 40 m sands) and 20% (420 m Jurassic/Triassic layer) porous

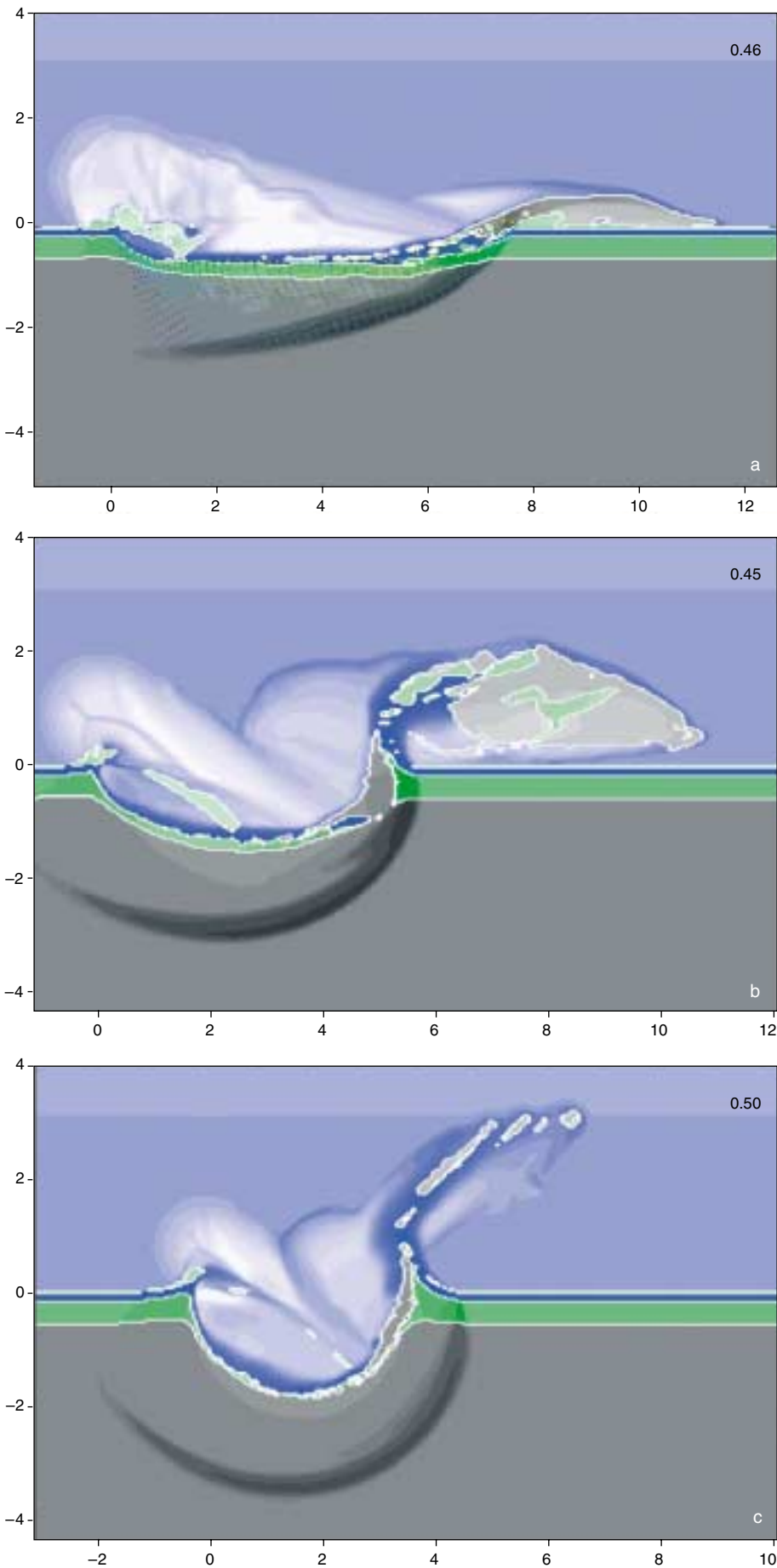


Figure 2. Initial stages (~0.5 seconds) of impact simulations for various impact angles: a) 15°, b) 30°, and c) 45°, for a 20 km/s impact (Table 4). The basement is shown in gray, quartzite in green, calcite in dark blue, and atmosphere is shown in light blue. All colors are graded according to density variations.

quartzite the ANEOS-based shock pressure for complete melting is 20 and 32 GPa, respectively, while it is 40 and 52 GPa for incipient vaporization. Finally, the ANEOS-based shock pressure for complete melting of granite (dense crystalline basement) is 56 GPa. These threshold pressures for melting and vaporization/de-gassing are modeled by ANEOS and may somewhat differ from those of real materials, although they are in fact very near to experimentally based estimates (e.g. see summary in Stöffler, 1984) which are 20 GPa for quartz sand, ~30 GPa for sandstone (25% porosity) and 60 GPa for granite. Volatiles may also strongly influence melt pressure values (at least the upper sand layer was water-saturated).

The results of simulations (Table 3) indicate that overall melt production is maximized for a 30°, 20 km/s impact. This emphasizes in particular the trade off between impact velocity and projectile size needed at various angles to keep a constant transient crater diameter. The decrease in projectile size eventually counteracts the increase in impact velocity by focusing the impact energy on a smaller region (decreasing the projectile's footprint). As a result, impact velocity appears to play a small role in impact melting of the uppermost layer, from which tektites originate (e.g. a 45° impact produces about 0.21–0.23 km³ of melt regardless of the impact velocity used in the simulations). On the other hand, impact angle is very important: lower impact angles dramatically increase the melting of the top layer (e.g. from 0.23 km³ for a 45° impact to 0.67 km³ for a 15° impact, at 20 km/s). These results suggest the need for a different approach for melt production from specific target layers compared to overall target melt.

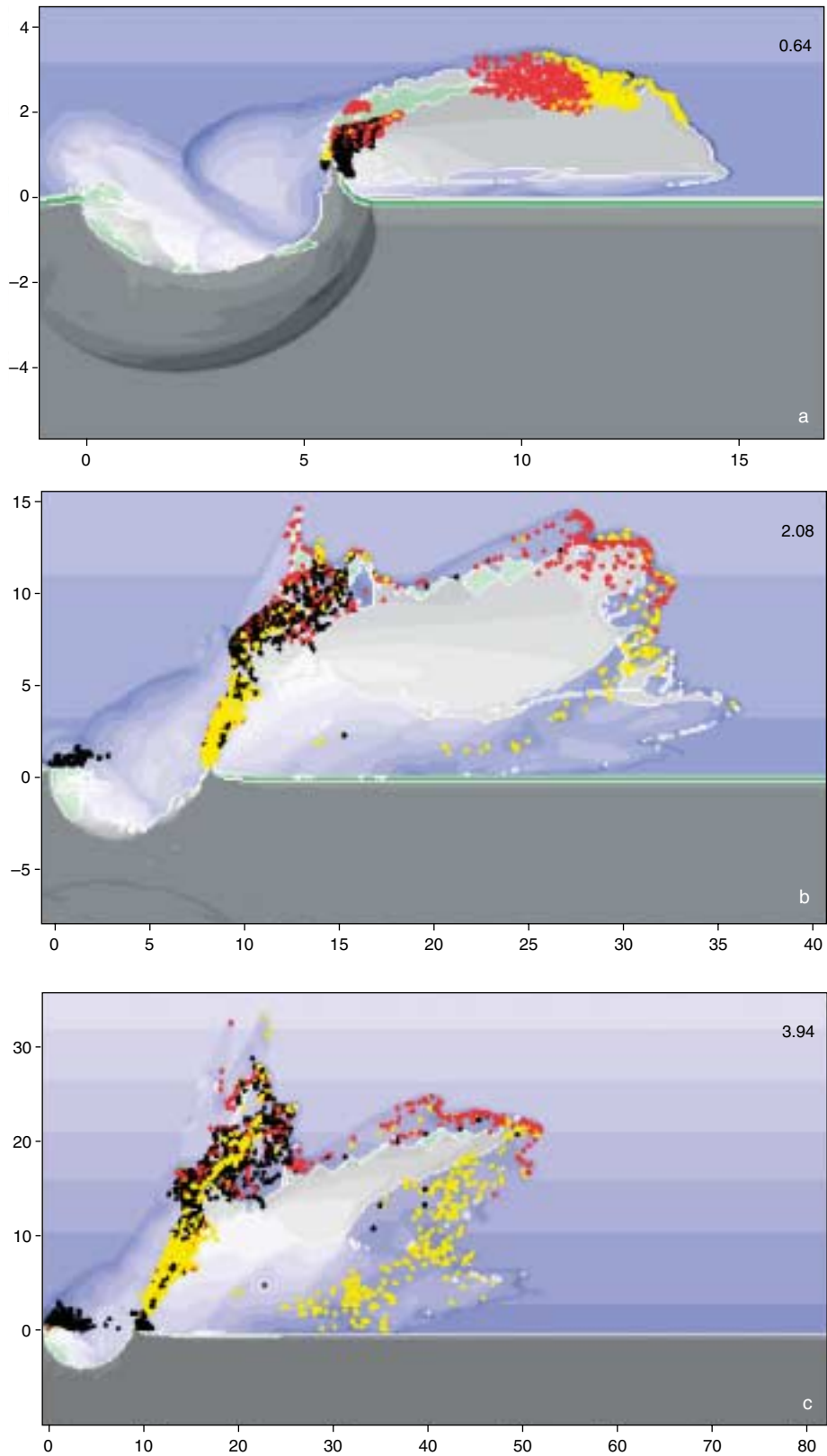


Figure 3. Tektite ejection model results for a 30° impact and impact speed of 20 km/s at a) 0.6 sec, b) 2 sec, and c) 3.9 sec. after the impact. ● – molten upper layer material (possible tektites); ● – molten target materials (not tektites); ● – solid target material.

Keeping projectile size constant, we have maximum target melt for vertical impact (Pierazzo and Melosh 1999),

while keeping crater size constant (and changing projectile size according to scaling laws by Schmidt and Housen 1987) we have maximum melt at 30°, followed by a sharp decrease at lower impact angles (Ivanov and Artemieva 2001). However, this 30° maximum may be explained by a sharp decrease in melt production from deep layers, not from the top one, which gives rather small input in overall melt. Nevertheless, exactly this top layer of sands is of crucial importance for tektite production. Finally, we choose the impact angle of 30° to model tektites.

Tektite production

Separate simulations have been carried out to investigate the formation and distribution of tektites formed in the Ries impact event. Previous modeling of this very particular case of impact ejecta dealt mainly with the initial stage of the impact–shock compression of the surface material and its acceleration after decompression (Artemieva 2001, 2002). These early runs showed that tektites (or, more accurately, high-velocity, high temperature target melt) might be produced by high-velocity (>15 km/s) impacts into silica-rich targets with impact angles between about 30° and 50° (Artemieva 2001, 2002). Very oblique impacts are not as efficient, and produce target melt that is strongly contaminated with projectile material. The main conclusion of the previous modeling work is that there is no need for special impact conditions to produce tektites (Artemieva 2002). The rather quick degradation of natural glasses can explain the relative tektite deficiency in the impact record: 4 tektite strewn fields versus more than 150 terrestrial impacts structures identified so far. Indeed, only young (< 50 Ma) craters have been associated with tektite strewn fields. The Ries is one of them, being associated with the well-known moldavite strewn field (Bohemia, Moravia, Lusatia, and Lower Austria).

The previous modeling effort treated molten material as a continuum (Artemieva 2002). This is a reasonable assumption in the early stages of crater growth and material ejection, but at some later stages the properties of individual particles (i.e. mass, size, shape, individual velocity) become important. At that point the particle trajectories in the atmosphere should be defined by the hydrodynamics of two phases, including the interaction (based on momentum and heat exchange) of solid (molten) particles with the post-impact gas flow. The size and shape of individual particles are influenced by many processes (e.g. Melosh and Vickery 1991, Melosh 1984, O’Keefe and Ahrens 1986); ideally, they should be modeled by adding a disruption module to the hydrocode. In our simplified approach, material disruption is assumed to occur when the density of the solid or molten material drops below the normal density for a given temperature within a single computational cell (i.e. the material is subject to tension). To start particle description we should define the particles’ properties, i.e. its initial position, velocity, size and shape.

The hydrodynamic velocity of the cell gives the initial particle velocity, while the object’s initial position within the cell is randomly defined. We have modeled solid particles size distribution by using an empirical size distribution based on experimental studies of high energy chemical explosions, with particle sizes ranging from ~ 1 µm to 10 cm. The diameter of molten particles lies in the range of 1–3 cm, which corresponds to the average size of tektites (O’Keefe 1963, 1976, Montanari and Koeberl 1999), while particle size drops to 0.01 cm if particles are produced by condensation from a two-phase mixture, where vapor and melt coexist (microtektites). These assumptions are based on a simple approach (Melosh and Vickery 1991): particle size in the melt disruption process depends on the balance of local strain rates and surface tension in the melt. Higher temperature melt has a smaller surface tension thus producing smaller particles. In our simplified approach, we model 3 cm-diameter particles if the temperature is around melting (1400–1500 K), and linearly decrease their size with increasing temperature, up to 1 cm-diameter particles around vaporization (~2800 K). If the particles are formed from vapor (condensation) they should be orders of magnitude smaller (Zeldovich and Raizer 1967). For simplicity, we model particles as ideal spheres (although this is not really the case for tektites).

The disruption of molten material within one computational cell with volume of $1.25 \times 10^5 \text{ m}^3$ ($50\text{m} \times 50\text{m} \times 50\text{m}$) will give about 10^{10} cm-diameter particles. To avoid limitations due to computer capacity, we have implemented the approach of using representative tracer particles (e.g. Teterov and Nemtchinov 1993, Shuvalov 1999, 2001): each tracer describes the motion of a large number (10^5 – 10^{10}) of real particles, all with the same properties (mass, shape, velocity and trajectory). This means that in the disruption process we produce huge amounts of particles (conserving mass), but then we solve a much smaller amount of equations to represent the tracers, each representing not a single particle but a group of particles with identical initial properties and therefore identical trajectories.

After disruption, each particle of mass m and diameter d is subject to gravity and drag forces. The equation of motion can be written as follows:

$$m \frac{du}{dt} = mg + 3\pi d\mu (u_g - u) + \frac{1}{4} C_d \pi d^2 \rho_g (u_g - u)^2,$$

where u and u_g are particle and gas velocity, respectively, ρ_g and μ are gas density and viscosity, and C_d is drag coefficient. The first term on the right represents gravity, the second represents Stokes’ drag, which is particularly important for low-velocity particles, and the third represents drag in high-velocity flow. In the absence of gas flow, the balance of Stokes’ drag and gravity defines the precipitation velocity of the particle, u_p :

$$u_p \pi = \frac{gd^2 \rho}{18\mu},$$

that depends on particle’s density ρ and diameter d , and gas viscosity μ . Its value varies from a few cm/s for

small, mm-sized particles to tens of m/s for cm-sized tektites (toward the final stages of the computations). Thus, a ballistic motion, which takes into account only gravity, is a simplified example of particle motion in a post-impact flow.

In this stage, the hydrodynamic model consists of two steps: the first is a standard update of the hydrodynamic values; the second is a calculation of each tracer's trajectory followed by an update of the hydrodynamic values to conserve momentum and energy. Particles move from cell to cell and finally may escape the Earth's gravity field or are deposited on the surface.

Figure 3 shows early stages of a Ries-type impact at 30° and 20 km/s, with particle production and motion in the atmosphere. Only particles larger than 1 cm in diameter are shown, to avoid an overload of the figure. Molten particles from the upper (40 m) quartzite layer (i.e. potential tektites) are shown in red, particles from the molten projectile or deeper target layers are yellow, and solid particles are shown in black. An appreciable part of the upper layer material is vaporized and it initially starts to move as a gas or two-phase mixture; later on, however, condensation from the vapor can occur, resulting in the formation of microtektites. There is no record of microtektites associated with the Ries crater. Microtektites are typically found in deep sea sediments where they are buried and therefore preserved; however, when exposed at the surface they are subject to strong weathering processes that destroy them.

The Ries impact site is characterized by a thick sedimentary layer, from which a large amount of vapor (e.g. CO_2) is shock-released. This vapor contributes to the particles acceleration, or at least, to maintaining their motion. The initial ejection velocities of material are rather high, up to 10 km/s, which is close to the velocity of the expanding gas. As a result, the particles are not subject to high dynamic pressures (Fig. 4a) that otherwise would disrupt them into fine mist immediately after ejection. The temperature of the entraining gas is rather high, so the particles do not cool quickly during the flight (Fig. 4b), thus having enough time to be aerodynamically shaped (typical for tektites), and to lose volatiles (like water). Four seconds after the impact, practically all of the molten and vaporized upper layer (sand) material is ejected and disrupted into particles, while intensive ejection of (either molten or solid) material from deeper layers will continue for much longer.

The initial hydrocode simulations, that include both the opening of the cavity and the atmospheric flow of material ejected from it, is performed to about 5 seconds after impact (Fig. 3). This initial stage is carried out at high spatial resolution and limited to a restricted mesh around the impact point, to obtain a reliable modeling of crater formation. On the other hand, to resolve the atmospheric flow of the expanding vapor plume and the imbedded particles we must model a rather large region – hundreds of kilometers in height and in the downrange direction, which can only be done at a much lower spatial resolution. This

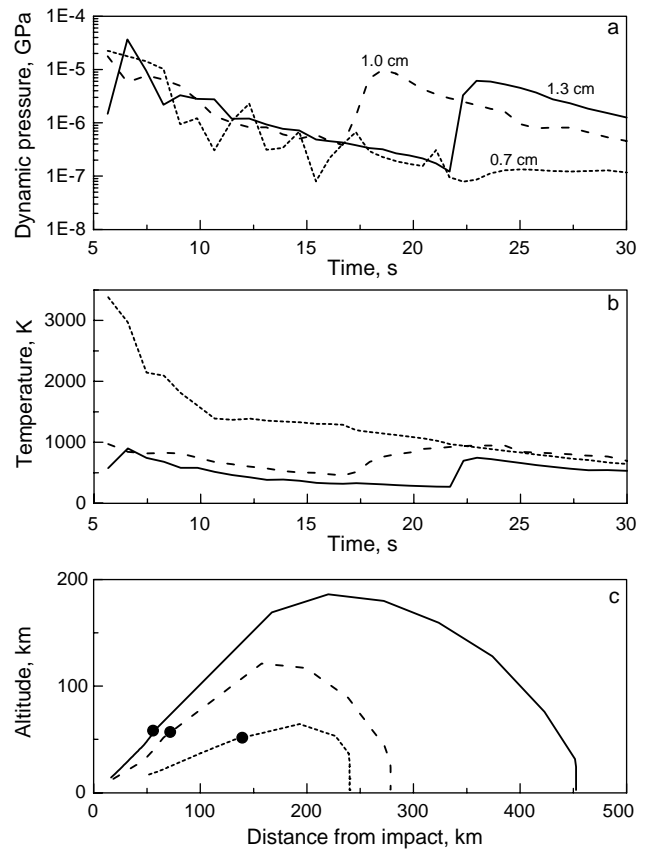


Figure 4. a – Dynamic pressure versus time for a few tektite-type particle of different sizes. The solid line represents a tektite 2.6 cm in diameter, dashed line a tektite 2.0 cm in diameter, and dotted line a tektite 1.4 cm in diameter. b – Temperature versus time for the same tektite-type particles of Fig. 7. c – Trajectories of the tektite-type particles shown in Figs 4a and 4b. Circles mark the end of the hydrodynamic simulations (~30 seconds after the impact). From that point on the trajectories represent the motion of particles in an undisturbed atmosphere.

affects our ability to model accurately low-velocity ejecta, but does not affect high-velocity ejecta.

Between 20 to 40 seconds after the impact, the majority of the particles has reached altitudes above ~ 50 km. We exclude from the model particles exceeding altitudes of ~ 200 km, corresponding to material that will reach worldwide distribution (furthermore, some of these particles have velocities above escape). At this point, a full-scale hydrocode modeling becomes computationally too expensive, becoming thus very inefficient (typical time step in the hydrocode simulation is less than 0.1 s). We then turn off the hydrodynamic flow and consider the motion of particles in an undisturbed atmosphere (i.e. using pre-impact stratification and zero gas velocity). The particles end up moving through the undisturbed atmosphere with low velocity (tens of meters per second, typical settling velocity for particles of that size and shape). Figures 4a-c show the complete trajectories of the tektite-type particles and the pressure-temperature condition along these trajectories. It usually takes 5–30 min for particles to land on the surface.

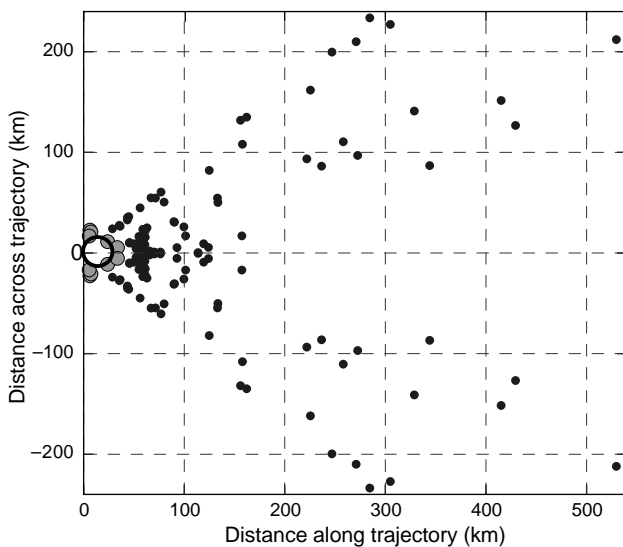


Figure 5: Final distribution of tektite-type particles on the surface for a 30° , 20 km/s impact. The origin is located at the impact point. Black and gray points represent mass of material deposited at a given location: black are for masses in the range 0.01–0.1 Mt; grey are for 0.1–2.0 Mt. The circle roughly corresponds to the rim of the Ries crater (its center is located not at the point of impact, but downrange because of impact obliquity).

The final surface distribution of the modeled tektites is shown in Fig. 5, where different color dots represent different tektite masses. The symmetry with respect to the downrange direction is a direct consequence of the bilateral symmetry adopted for the simulation. About 1.6×10^{10} kg of tektites are deposited in the simulation. A fraction of this material ($\sim 6 \times 10^9$ kg) lands close to the impact point, indicating it is part of the ejecta curtain that surrounds the crater (usually extending about two radii away from the crater). The remaining $\sim 10^{10}$ kg could be identified as tektites. This estimate differs by only a factor of 2 from geological estimates of $\sim 5 \times 10^9$ kg (e.g. Montanari and Koeberl 1999). The tektite-type material is distributed up to 400–500 km away from the impact, in a fan of $\sim 75^\circ$ symmetrically distributed with respect to the downrange direction. The final distribution of tektites is in principle but not in detail similar to the distribution of the real moldavites. This indicates that the production and distribution of tektites can be explained by impact cratering mechanics and the physics of motion of particles in a gas flow.

Summary and discussion

On the basis of a detailed assessment of the geological, petrographic and geographical characteristics of the related impact phenomena – Ries–Steinheim craters and the moldavite tektite strewn field – a numerical modeling study has been performed under the assumption that an impact of binary asteroid most probably was responsible for the formation of these two craters and the tektites because of their

identical age. The total calculated mass of landed tektites is near 10^{10} kg which compares with the 5×10^9 kg estimated from field observations (Montanari and Koeberl 1999). It is obvious from the results that the 3D numerical simulation of the impact and ejection processes can explain the observations with a relatively good precision. The detailed arguments for the model-based interpretation of the field observations are as follows.

The results of a series of 3D hydrocode simulations of a Ries-type impact (i.e. maintaining a constant transient crater) for different impact angle and impact velocities confirm previous results indicating 30° as the most favorable angle for near-surface melting and low projectile material contamination, and, consequently, for the formation of tektites. Impact velocity has a smaller influence on the amount of melt and vaporization, compared to impact angle (Table 3).

The modeling of the motion of impact-produced tektite-type particles through the atmosphere addresses mainly the “mechanical” component of the complex tektite problem that is the possibility of transferring particles hundreds of km away from the parent crater. At this point, we cannot address the “geochemical” component of the problem in detail although the calculated P-T-conditions (Figs 4a, b) can explain some characteristics, such as low water content, homogeneity and scarcity of vesicles of tektites. A simulation of a Ries-sized impactor at 30° , 20 km/s, produces a downrange, relatively narrow-angle, distant distribution of tektite-type material similar to that observed for the moldavite strewn field. Although the final particle distribution appears to be somewhat different from the known distribution of the moldavites, these results represent an important step toward a better understanding of the moldavite strewn field. The exact width of the fan, $\sim 75^\circ$ for the modeled 30° impact, is a function of impact angle; to characterize such a dependence requires to extend the (time and computationally) extensive simulation carried out for a 30° impact to other impact angles in the range of 20° – 50° . However, we expect that this value will not vary abruptly in the accepted range. The lack of tektites in the range of up to 200 km in contrast to the calculation is easily explained by the lack of host sediments of the age of the Ries in the whole region between the Ries and the western border region of the Czech Republic. Several other factors could have influenced the final distribution of the moldavites. Besides projectile-related factors, such as projectile size, impact angle and impact velocity, target characteristics like local variations in the stratigraphy and a discontinuous distribution of the upper layer of Tertiary sands in the Ries, and the size distribution of the melt particles are likely to affect the final distribution of the moldavites. The fact that the fan where the moldavites are found now has an angle of 57° compared to the 75° angle resulting from the calculation may be also due to erosion and surface transport of tektites since their formation.

References

- Ahrens T. J., O'Keefe J. D. (1977): Equations of state and impact-induced shock wave attenuation on the Moon. In: Roddy D. J., Pepin R. O., Merrill R. B. (eds) *Impact and Explosion Cratering*. 639–656, Pergamon Press, New York, USA.
- Artemieva N. A. (2001): Tektite production in oblique impacts. *Lunar Planet. Sci. Conf.* 32, Abstr. #1216, Houston, TX.
- Artemieva N. A. (2002): Tektite origin in oblique impact: Numerical modeling. In: Koeberl C., Plado J. (eds) *Impacts in Precambrian shields*. Springer-Verlag, Berlin, pp. 257–276.
- Artemieva N. A., Shuvalov V. V. (1994): Oblique impact: Atmospheric effects. *Lunar Planet. Sci. Conf.*, 25, 39–40, Houston, TX.
- Artemieva N. A., Shuvalov V. V. (2001): Motion of fragmented meteoroid through the planetary atmosphere. *J. Geophys. Res.* 106, 3297–3310.
- Bolten R., Müller D. (1969): Das Tertiär im Nördlinger Ries und in seiner Umgebung. *Geologica Bavarica* 61, 87–130.
- David E. (1966): Flight of tektites from meteorite impact. *Z. Naturforsch.* 21a, 1131–1137.
- Engelhardt W. von (1997): Suevite breccia of the Ries impact crater, Germany: Petrography, chemistry, and shock metamorphism of crystalline clasts. *Meteoritics and Planet. Sci.* 32, 545–594.
- Engelhardt W. von, Stöffler D., Schneider W. (1969): Petrologische Untersuchungen im Ries. *Geologica Bavarica* 61, 229–295.
- Engelhardt W. von, Luft E., Arndt J., Schock H., Weiskirchner W. (1987): Origin of moldavites. *Geochim. Cosmochim. Acta* 51, 1425–1443.
- Gall H., Müller D. (1975): Reutersche Blöcke – ausseralpine Fremdgesteine unterschiedlicher Herkunft in jungtertiären und quartären Sedimenten Südbayerns. *Mitt. Bayer. Staatssamml. Paläontol. Hist. Geol.* 15, 207–228.
- Gentner W., Wagner G. A. (1969): Altersbestimmungen an Riesgläsern und Moldaviten. *Geologica Bavarica* 61, 296–303.
- Gentner W., Lippolt H. J., Schaeffer O. A. (1963): Argonbestimmungen an Kaliummineralien – XI. Die Kalium-Argon-Alter der Gläser des Nördlinger Rieses und der böhmisch-mährischen Tektite. *Geochim. Cosmochim. Acta* 27, 191–200.
- Graup G. (1978): Das Kristallin des Nördlinger Ries. *Petrographische Zusammensetzung und Auswurfsmechanismus der kristallinen Trümmernmassen, Struktur des kristallinen Untergrundes und Beziehungen zum Moldanubikum*. Ferdinand Enke Verlag, Stuttgart, 190 pp.
- Horn P., Mueller-Sohnius D., Koehler H., Graup G. (1985): Rb-Sr systematics of rocks related to the Ries, Germany. *Earth Planet. Sci. Lett.* 75, 384–392.
- Hüttner R., Schmidt-Kaler H. (1999): Erläuterungen zur geologischen Karte des Rieses 1 : 50000. *Geologica Bavarica* 104, 7–76.
- Ivanov B. A., Artemieva N. A. (2001): Transient cavity scaling for oblique impacts. *Lunar Planet. Sci. Conf.* 32, Abstr. #1327, Houston, TX.
- Koeberl C., Brandstätter F., Niedermayer G., Kurat G. (1988): Moldavites from Austria. *Meteoritics* 23, 325–332.
- Lange J.-M. (1990): Tektite der Niederlausitz; Natur und Landschaft Bezirk Cottbus NLBC, 12, 77–94.
- Lange J.-M. (1996): Tektite glasses from Lusatia (Lausitz), Germany. *Chemie der Erde* 56, 498–510.
- McGlaun J. M., Thompson S. L., Elrick M. G. (1990): CTH: A three-dimensional shock wave physics code. *Int. J. Impact Eng.* 10, 351–360.
- Melosh H. J. (1984): Impact ejection, spallation, and the origin of meteorites. *Icarus* 59, 234–260.
- Melosh H. J., Vickery A. M. (1991): Melt droplet formation in energetic impact events. *Nature* 350, 494–497.
- Montanari A., Koeberl C. (1999): *Impact stratigraphy: The Italian Record*. Springer-Verlag (Berlin – Heidelberg) 364 pp.
- O'Keefe J. A., ed. (1963): *Tektites*. Univ. Chicago Press, Chicago, IL, 228 pp.
- O'Keefe J. A. (1976): *Tektites and their origin*. Elsevier, New York, NY, 254 pp.
- O'Keefe J. D., Ahrens T. J. (1977): Impact-induced energy partitioning, melting, and vaporization on terrestrial planets. *J. Geophys. Res.* 92, 1849–1870.
- O'Keefe J. D., Ahrens T. J. (1986): The size distributions of fragments ejected at a given velocity from impact craters. *Lunar Planet. Sci. Conf.* 17, 1004–1005, Houston, TX.
- Pierazzo E., Melosh H. J. (1999): Hydrocode modeling of Chicxulub as an oblique impact event. *Earth Planet. Sci. Lett.* 165, 163–176.
- Pierazzo E., Melosh H. J. (2000): Melt production in oblique impacts. *Icarus* 145, 252–261.
- Pierazzo E., Vickery A. N., Melosh H. J. (1997): A reevaluation of impact melt production. *Icarus* 127, 408–423.
- Pierazzo E., Kring D. A., Melosh H. J. (1998): Hydrocode modeling of the Chicxulub impact event and the production of climatically active gases. *J. Geophys. Res.* 103, 28 607–28 625.
- Pohl J., Stöffler D., Gall H., Ernstson K. (1977): The Ries impact crater. In: Roddy D. J. et al. (eds) *Impact and Explosion Cratering*. Pergamon Press, New York, pp. 343–404.
- Reiff W. (ed.) (1979): *Guidebook to the Steinheim Basin Impact Crater*, Geol. Landesamt Baden-Württemberg, Stuttgart, 32 pp.
- Schmidt R. M., Housen K. R. (1987): Some recent advances in the scaling of impact and explosion cratering. *Int. J. Impact Eng.* 5, 543–560.
- Shuvalov V. (1999): Multi-dimensional hydrodynamic code SOVA for interfacial flows: Application to the thermal layer effect. *Shock Waves* 9, 381–390.
- Shuvalov V. (2001): Dust ejection induced by small meteoroids impacting Martian surface. *Lunar Planet. Sci. Conf.* 32, Abstr. #1126, Houston, TX.
- Staudacher T., Jessberger E. K., Dominik T. K., Schaeffer O. A. (1982): ⁴⁰Ar-³⁹Ar ages of rocks and glasses from the Nördlinger Ries crater and the temperature history of impact breccias. *J. Geophys.* 51, 1–11.
- Stöffler D. (1984): Glasses formed by hypervelocity impact. *J. Non-Cryst. Solids* 67, 465–502.
- Stöffler D., Ostertag R. (1983): The Ries impact crater. *Fortschr. Mineral.* 61, B2, 71–116.
- Stöffler D., Artemieva N. A., Pierazzo E., Ivanov B. A. (2001): Ries crater, Germany: Geology and numerical modeling of impact cratering. *Meteorit. Soc. Conf.* 64, Abstr. #5180, Rome, Italy.
- Stöffler D., Artemieva N. A., Pierazzo E. (2002): Modeling the Ries-Steinheim impact event and the formation of the moldavite strewnfield. *Lunar Planet. Sci. Conf.* 33, Abstr. #1871, Houston, TX.
- Teterev A. V., Nemtchinov I. V. (1993): The sand bag model of the dispersion of the cosmic body in the atmosphere. *Lunar Planet. Sci. Conf.* 24, 1415–1416, Houston, TX.
- Thompson S. L., Lauson H. S. (1972): Improvements in the Chart D Radiation-Hydrodynamic Code III: Revised analytical equation of state. SC-RR-61 0714, 119 pp. Sandia Nat. Labs. Albuquerque, NM.
- Vand V. (1963): Ries Kessel and Steinheim Basin. *Mineral industries expt. Sta., Pennsylvania* 32(4), 1–8; also referenced on p. 300 and 301, in Preuss E. (1964) *Das Ries und die Meteoritentheorie*. *Fortschritte Mineralogie*, 41, 271–312.

Handling editor: Roman Skála